JOURNAL OF Materials CHEMISTRY

Synthesis, structural and chemical properties of iron oxide–silica aerogels†

Patrizia Fabrizioli,[a] Thomas Bürgi,[a] Marco Burgener,[a] Sabine van Doorslaer[b] and Alfons Baiker*[a]

[a]*Laboratory of Technical Chemistry, Swiss Federal Institute of Technology, ETH Hönggerberg-HCI, CH-8093 Zürich, Switzerland. E-mail: baiker@tech.chem.ethz.ch; Fax: +41 1 632 11 63; Tel: +41 1 632 31 53*
[b]*Laboratory of Physical Chemistry, Swiss Federal Institute of Technology, ETH Hönggerberg-HCI, CH-8093 Zürich, Switzerland*

Received 7th September 2001, Accepted 6th December 2001
First published as an Advance Article on the web 4th February 2002

Iron oxide aerogels were synthesized from tetramethoxysilicon(IV) (TMOS) or tetraethoxysilicon(IV) (TEOS) and iron nitrate using an acid-catalyzed solution–sol–gel method combined with subsequent extraction of the alcoholic solvent with supercritical CO_2. The main parameters varied in the sol–gel synthesis were: the type of N-base used as the gelation agent (*N,N*-diethylaniline, trihexylamine, ammonium carbonate, ammonia), the concentration of the iron precursor, and the water content. The silicon precursor was prehydrolyzed to improve its reactivity. After calcination at 600 °C, the structural and chemical properties of the aerogels containing 0–20wt% nominal Fe_2O_3 were characterized by means of nitrogen adsorption, X-ray diffraction (XRD), transmission and scanning electron microscopy, temperature programmed reduction, X-ray photoelectron spectroscopy (XPS), UV-Vis, DRIFT and EPR spectroscopy. XRD and electron microscopy indicated that all aerogels were amorphous, irrespective of the sol–gel conditions used. The aerogels were predominantly mesoporous, with pore size maxima ranging between 20–50 nm, but also exhibited some microporosity. For the 10 wt% iron oxide samples, the specific pore volumes ranged from 0.7 to 2 $cm^3\ g^{-1}$ and BET-surface areas from 150 to 636 $m^2\ g^{-1}$, depending on conditions. With increasing iron content, the BET surface area decreased from 740 to 340 $m^2\ g^{-1}$, accompanied by increasing microporosity. XPS revealed significant silicon enrichment on the surface. Spectroscopic investigations (UV-Vis, EPR) uncovered different iron-containing species, ranging from tetrahedrally coordinated iron atoms incorporated in the silica matrix to iron oxide nanoclusters. Formation of isolated iron atoms was favored with low iron content samples. The N-base used to force gelation had a significant effect on the morphology and population density of Fe(OH)Si in the aerogels.

1 Introduction

Mixed oxides play a central role in chemical and petrochemical processing as catalysts and as supports for catalytically active species. Particularly attractive are aerogels, which are high surface, high porosity materials prepared by the sol–gel method combined with subsequent supercritical extraction. In addition to their various catalytic uses, aerogels have applications in many other areas, such as insulation and ceramics.[1,2] Preparation of catalytic mixed oxides by sol–gel chemistry affords a degree of control over the intimacy of molecular-scale mixing and the textural properties, which is hardly achievable by other methods. Also, compared to crystalline materials, aerogels can offer higher flexibility with regard to chemical composition. However, an inherent problem of sol–gel-derived materials is that mixing of the constituents on the molecular scale is difficult to achieve and the resulting structures are often metastable, prone to restructuring.[3,4] A survey of the various aerogels which have been applied in catalysis, together with the corresponding reactions they catalyze, has been given in recent reviews.[4–6]

There are only few reports in the literature on Fe–Si mixed oxide xero- and aerogels. Iron oxide silica xerogels containing iron oxide nanoparticles were synthesized by the sol–gel method in view of the novel magnetic, optical and chemical properties of these materials.[7–10] To the best of our our knowledge, all iron oxide-containing aerogels reported so far were dried at high temperature, which readily induces segregation of the mixed oxide constituents. Syntheses of Fe_2O_3–Al_2O_3[11,12] and Fe_2O_3–SiO_2 high temperature aerogels[12–14] have been reported. Wang and Willey[15] synthesized high temperature Fe_2O_3–SiO_2 aerogels for the oxidation of methanol. Willey and co-workers prepared iron oxide–chromia–alumina high temperature aerogels,[16] as well as magnesium oxide–iron oxide spinel aerogels[17] for the selective catalytic reduction of NO by ammonia. The catalytic potential of iron–silicon oxide materials, most prominently represented by the family of Fe–silicalites, has been investigated for a variety of catalytic reactions, ranging from petrochemical[18] to environmental catalysis, such as selective catalytic reduction (SCR) of NO_x by ammonia,[19–21] SCR by hydrocarbons[22–25] and N_2O decomposition.[26,27]

Characterization of the iron-containing zeolites and iron oxide–silica mixed oxides is complex due to the many possible states of the Fe^{3+} ion, ranging from tetrahedrally or distorted tetrahedrally coordinated Fe^{3+} incorporated in the framework over binuclear iron complexes[28] to octahedrally coordinated iron ions in iron oxide particles.[24,29–32] Due to the wide variety of possible iron species found for ferrisilicalites, the result of a single characterization method may be ambiguous.[29,33] We applied therefore a series of different characterization methods.

In the following, we report the synthesis of high surface area, mesoporous iron–silicon mixed oxide aerogels suitable for

†Electronic supplementary information (ESI) available: cumulative pore volumes and *t*-plots of the calcined aerogels prepared by different sol–gel methods, and of aerogels with different iron loadings. See http://www.rsc.org/suppdata/jm/b1/b108120a/

catalytic applications. In doing so, we examined the effects of changing sol–gel parameters, such as base used as gelation agent, concentration of iron precursor, and type of silicon precursor, on the structural and chemical properties of the aerogels. In addition, the effect of heat treatment on the final aerogel characteristics was investigated. From the results, it emerges that the properties of the iron–silicon mixed oxides are strongly dependent on the choice of preparation conditions. Iron dispersion is particularly sensitive to the iron content and the temperature treatment, whereas the acidic properties are greatly influenced by the type of base used as the gelation agent.

2 Experimental

2.1 Preparation of aerogels

Iron–silicon mixed oxide aerogels were prepared by the solution-sol–gel (SSG) route applying different conditions. Tetramethoxysilicon(IV) (TMOS; Fluka, puriss.) and tetraethoxysilicon(IV) (TEOS; Fluka, puriss.), and $Fe(NO_3)_3{\cdot}9H_2O$ (Fluka, puriss.) were the precursors. Some synthesis parameters are summarized in Table 1. The aim of the synthesis was to achieve highly disperse iron oxide–silica mixed oxides with high surface area. The synthesis route described for the preparation of high temperature Fe_2O_3–SiO_2 aerogels from $Fe(acac)_3$ precursor[12,14,15,34] was not successful. During low temperature drying, the iron precursor was extracted with the alcohol, since $Fe(acac)_3$ was not hydrolyzed in dilute acid media.[35]

The precursor chosen here was therefore iron(III) nitrate. The 3+ oxidation state of iron is stable in solution in the presence of oxygen donating ligands.[35] In order to adjust the different hydrolysis rates of the iron and silicon precursors, TEOS was prehydrolyzed. Solvated Fe^{3+} ions were reported to form stable complexes with monomeric and low polymerized silica.[36] As intensively studied for single oxide sols, pH and water content strongly influence stiffness, morphology and the chemical properties of the final product.[3] Base type, base and water concentration, iron concentration and silicon precursor were varied in order to avoid precipitation of the sol and to reach the gel point within a reasonable period of time.

The sol was prepared as follows: 34.4 g tetramethoxysilicon(IV) (TMOS; Fluka, puriss.) was dissolved in 20 ml methanol (MeOH; Fluka, puriss.). For the hydrolysant, nitric acid (HNO_3, 65%, Merck, p.a.) and bidistilled water were mixed in the molar ratio $H_2O : H^+ = 4 : 0.01$, and 16.60 g was dissolved in 10 ml MeOH. The hydrolysant was then added to the TMOS solution *via* a dropping funnel for 30 min under vigorous stirring, resulting in a molar ratio $H_2O : H^+ :$ TMOS of $4 : 0.01 : 1$. The temperature of the clear solution increased to about 50 °C. After 30 min, the solution was cooled down and 20 ml MeOH were added. In a baker, 7.75 g $Fe(NO_3)_3{\cdot}9H_2O$ (Fluka, puriss.) was dissolved in 30 ml MeOH. The solution was added to the prehydrolyzed silicon precursor. The yellow–orange clear sol was aged for 40 h. For gelation, different nitrogen-containing bases were used. The acronyms for the gels are chosen according to their preparation procedures. The first numeral refers to the nominal Fe_2O_3 content in wt%, based on the theoretical system Fe_2O_3–SiO_2 (10 wt% "Fe_2O_3' = 7.0 wt% Fe = 2.6 at% Fe). Since most gels were prepared with a nominal composition of 10 wt% Fe_2O_3/90 wt% SiO_2 the iron content of these samples is omitted in the corresponding acronym. The subsequent capital letters describe the sol–gel route applied: first, the silicon precursor is given, M (E) indicating that tetramethoxysilicon (tetraethoxysilicon) was used. Then, the gelation agent is represented by two to four letters, as detailed in the following paragraphs. In the following brief descriptions of the different preparations are given and some synthesis parameters are listed in Table 1.

M/NN: 24 ml *N,N*-diethylaniline (Fluka, puriss.) was dissolved in 72 ml MeOH. The solution was added to the sol over the course of 2 h. After one more hour, a yellow–brown transparent gel was formed.

M/Tri: 18 ml trihexylamine (Fluka, purum > 99%) in 54 ml MeOH was added to the sol over the course of 1.5 h. Flocculation and re-dissolution was observed and a transparent gold–brown gel formed after 5 days.

M/NC: 6 g ammonium carbonate [$(NH_4)_2CO_3$, Semadeni] was dissolved in 36 ml bidistilled water before 150 ml MeOH was added. Again, the solution was dropped into the sol over the course of 2 h and a yellow–brown turbid gel immediately formed.

M/NCf (f = fast): analogously to sample M/NC, an ammonium carbonate–water–ethanol solution was used for gelation, which was added to the sol within 5 minutes. Immediately, a voluminous, white and beige, turbid gel formed.

M/NH$_3$: 2 ml of an aqueous ammonia solution (NH_4OH, *ca.* 25 wt% in water, Fluka, puriss.) was dissolved in 98 ml MeOH. The solution was added to the sol over the course of 1 h. The same procedure was repeated after 24 h and 48 h. The sol turned to a bright yellow soft gel after 2 days.

Md/NN (d = diluted): the amount of alcohol in the hydrolysis step was increased by a factor of two with respect to M/NN. 34.4 g TMOS was dissolved in 40 ml MeOH and the hydrolysant in 20 ml MeOH. Hydrolysis was carried out as described above. No alcohol was added after the hydrolysis step. The same gelation procedure as for M/NN was applied. Analogously to Md/NN with 10 wt% Fe_2O_3, gels with 5 wt% and 20 wt% Fe_2O_3 nominal content were prepared (5/Md/NN, 20/Md/NN). A pure silica gel (0/Md/NN) was also synthesized, in the course of which gelation occurred after addition of 70% of the basic solution.

Table 1 Parameters for the sol–gel synthesis of the iron–silicon mixed oxide aerogels

Aerogel[a]	Silicon precursor	Base	Base/mol	Basic solution[b]/ml	Gelation time after start of base addition
M/NN	TMOS	*N,N*-Diethylaniline	0.15	96	3 h
Md/NN[c]	TMOS	*N,N*-Diethylaniline	0.15	96	8 h
5/Md/NN	TMOS	*N,N*-Diethylaniline	0.15	96	7 h
20/Md/NN	TMOS	*N,N*-Diethylaniline	0.15	96	2.5 h
0/Md/NN	TMOS	*N,N*-Diethylaniline	0.10	69	1.5 h
M/Tri	TMOS	Trihexylamine	0.05	72	5 d
M/NC	TMOS	$(NH_4)_2CO_3$, 14 wt% in H_2O	0.06	186	2 h
M/NCf[d]	TMOS	$(NH_4)_2CO_3$, 14 wt% in H_2O	0.06	186	5 min
M/NH$_3$	TMOS	NH_4OH, 25 wt% in H_2O	0.04	300	5 d
E/NH$_3$	TEOS	NH_4OH	0.04	66	2 h
E/NH$_3$d	TEOS	NH_4OH	0.04	156	2 d

[a]Aerogel labelling is explained in the text. [b]The total volume of the basic solution, composed of the base, the alcohol, and water in some cases. [c]d stands for diluted, as more alcohol for the hydrolysis of the silicon alkoxide was used. [d]f stands for fast and refers to the speed of addition of the basic solution.

Gels based on tetraethoxysilicon(IV) (TEOS; Fluka, puriss.) were prepared by acid hydrolysis analogously to the TMOS-based materials. Gelation was forced by ammonia solutions, with higher ammonia concentration than in the corresponding M/NH_3 gel. Ammonia solutions with the same concentration resulted in precipitation of a TMOS-based sol, whereas a gel was obtained for the TEOS-based sol.

E/NH₃: for gelation, 6 ml of an aqueous ammonia solution (NH_4OH, 25 wt% in water, Fluka, puriss.) was dissolved in 60 ml EtOH. The solution was added to the sol over the course of 2 h. A brown gel formed immediately.

E/NH₃d (d = diluted): 6 ml 25% NH_3/H_2O was dissolved in 150 ml EtOH and added to the sol over the course of 2 h. After 2 days, a brown gel was formed.

Supercritical drying. Before drying, all gels were aged for 36–42 h under nitrogen at room temperature. For extraction with supercritical CO_2, the gels were transferred into a 2 dm^3 autoclave and covered with 90 ml of MeOH. Within 1 h and at a temperature of 313 K, the autoclave was pressurized with CO_2 to 22 MPa and the liquid–gas separator to 1 MPa, which required 2.1 kg of CO_2. The solvent of the solution–sol–gel (SSG) product was semicontinuously extracted for 6 h by a CO_2 flow of 20 g min^{-1}. Finally, the CO_2 was isothermally released at a rate of *ca.* 20 g min^{-1}.

Calcination procedure. 3 g of the raw aerogel powder was calcined in a tubular reactor with upward flow. The reported temperatures correspond to the oven temperatures. To remove part of the organic residues prior to calcination, all aerogel samples were heated in a nitrogen flow of 0.5 dm^3 min^{-1} at a rate of 5 °C min^{-1} to 200 °C and held at this temperature for 1 h. After cooling to *ca.* 80 °C, they were heated at 5 °C min^{-1} in air flowing at 0.5 dm^3 min^{-1} first to 200 °C and held for 2 h, then to 600 °C and held for 3 h.

Analogously to the calcination procedure described above, portions of Md/NN and 0/Md/NN were calcined at 900 °C for 1 h (Md/NN900 and 0/Md/NN900).

2.2 Physicochemical characterization

Atomic absorption spectroscopy (AAS). In order to determine the iron content of the calcined samples, 60 mg dry aerogel was dissolved in 200 µl hydrofluoric acid (HF, 40% in water, Fluka, 99.5%). The superfluous fluoride ions were neutralized with boric acid. The probe solution was diluted with bidistilled water and HCl to a stable solution of the iron ions with 90 ppm Fe and 0.1 mol kg^{-1} HCl, and analyzed on a VARIAN SpektrAA-10 atomic absorption spectrometer by comparison with standard solutions.

C, H, N analysis. Total carbon, hydrogen and nitrogen contents of the samples treated at 200 °C in air and after calcination at 600 °C were determined with a LECO CHN-900 elemental microanalysis apparatus.

Nitrogen physisorption. Prior to measurement, the samples were degassed to 0.1 Pa at 100 °C. Textural properties were determined by nitrogen physisorption at −196 °C using a Micromeritics ASAP 2000 instrument. The specific surface area (S_{BET}) was calculated in the relative pressure range 0.01–0.15, assuming a cross-sectional area of 0.162 nm^2 for the nitrogen molecule. The estimated *C* values were in the range 170–270 for the samples calcined at 600 and 900 °C, and about 120 for the samples treated at 200 °C. The specific desorption pore volume was assessed by the Barrett–Joyner–Halenda (BJH) method, which is assumed to cover the cumulative adsorption pore volume of pores in the maximum diameter range 1.7–300 nm. The assessment of microporosity was made from the *t*-plot constructions ($0.5 < t < 0.7$), using the Harkins–Jura correlation.

X-Ray diffraction (XRD). XRD measurements were performed on a Siemens D5000 powder X-ray diffractometer. The diffractograms were recorded with Cu-Kα radiation over the 2Θ range 15–65° and a position-sensitive detector with Ni filter.

UV-Vis spectroscopy: A Perkin-Elmer Lambda 16 spectrophotometer equipped with a 76 mm integrating sphere using $BaSO_4$ (Fluka; purum p.a.) as reference was applied to record the UV-Vis diffuse reflectance spectra of powder samples under ambient conditions. For measurements over the range 200–700 nm, the calcined aerogel powder was diluted (10 wt% in $BaSO_4$).

IR-spectroscopy. IR spectra were recorded on a Bruker IFS-66/S spectrometer at 4 cm^{-1} resolution. 1–2 mg samples were mixed with 100 mg KBr and spectra were measured under ambient conditions.

Diffuse reflectance infrared Fourier transform spectroscopy (DRIFTS). DRIFT spectra were recorded on a Perkin Elmer System 2000 FTIR instrument with a diffuse reflectance cell and a controlled environmental chamber (both Spectra-Tech) equipped with CaF_2 windows. The sample was mounted on a ceramic frit (Al_2O_3), and heated in a dried synthetic air stream (Pangas, 20% O_2 purity 99.5%, 80% N_2 purity 99.995%) to 300 °C for 1 h and spectra were recorded by accumulating 50 scans at a resolution of 4 cm^{-1}. The spectra in the reflection mode were transformed to the Kubelka–Munk function and normalized to the Si–O overtone vibration at 1848 cm^{-1}.[37]

Temperature programmed reduction (TPR). The apparatus used for TPR measurements has been described elsewhere.[38] An amount of sample corresponding to 0.2 mmol Fe was used for every analysis, taking into account the water content. The measurements were carried out using 5% hydrogen in argon as reducing gas and a flow-rate of 75 ml min^{-1}. Samples were pretreated in air at 550 °C for 30 min. The temperature during reduction was ramped from 25 to 1100 °C at 5 °C min^{-1}.

X-Ray photoelectron spectroscopy (XPS). XPS analysis was performed in a Leybold LHS 11 instrument. Mg-Kα radiation (240 W) was used to excite photoelectrons, which were detected with the analyzer operated at 31 eV constant pass energy, resulting in a line width of 0.9 eV (FWHM) for the $Ag3d_{5/2}$ line. The energy scale of the spectrometer was calibrated *versus* the $Au4f_{7/2}$, $Ag3d_{5/2}$ and $Cu2p_{3/2}$ lines of 84.2, 367.9 and 932.4 eV. Correction of the energy shift, due to steady-state charging was accomplished by taking the C1s line from adsorbed hydrocarbons at 285.0 eV as an internal standard. Empirically derived atomic sensitivity factors were used for quantification.[39]

Electron microscopy. For transmission electron microscopy (TEM), the calcined and ground aerogel was deposited on a holey carbon foil supported by a copper grid. The Phillips CM30 microscope, operated at 300 kV, was equipped with a supertwin lens (cs = 1.2 mm, point resolution < 0.2 nm). Scanning electron microscopy (SEM) was performed on a Hitachi S-900, operated at $V = 15$ kV. Samples were prepared as for the TEM measurements.

Continuous wave electron paramagnetic resonance spectroscopy (EPR). The X-band spectra were recorded on a Bruker ESP 300 spectrometer (microwave frequency 9.43 GHz), equipped with a ER4131 VT digital temperature control system making use of gaseous nitrogen as the coolant. All spectra were measured at room temperature and at −137 °C. A microwave power of 20 mW, a modulation amplitude of 0.5 mT and a modulation frequency of 100 kHz were used. Some samples were evacuated before analysis to 10 mbar and 0.01 mbar, respectively, for 4 h or to 10^{-6} mbar for 8 h.

3 Results

The main variables changed in the sol–gel synthesis were the type of N-base used as gelation agent, the concentration of iron precursor and the type of silicon precursor (see Table 1).

Table 2 Textural properties and C and N content of iron–silicon mixed oxide aerogels

Aerogel	Treatment in air/°C	S_{BET}/m^2 g^{-1}	S_{MP}[a]m^2 g^{-1}	V_P[b]/cm^3 g^{-1}	V_{MP}[c]/cm^3 g^{-1}	d_{max}[d]/nm	C content/wt%	N content/wt%
M/NN	200	192	0	1.29	0	52	15.2	1.9
	600	310	155	1.10	0.07	40	0.1	0.1
Md/NN	200	159	0	0.78	0	30	15.9	2.5
	600	300	166	0.72	0.07	23	0.1	0.1
Md/NN900	900	150	18	0.68	0.01	30	0.1	0.1
5/Md/NN	600	610	160	1.80	0.07	45	0.1	0.1
20/Md/NN	600	342	314	0.12	0.14	< 2	0.3	0.1
0/Md/NN	600	739	145	2.60	0.09	40	—	—
M/Tri	200	176	0	0.74	0	27	15.5	2.1
	600	335	138	0.72	0.05	20	0.1	0.1
M/NC	200	264	23	1.03	0.02	50	1.1	5.1
	600	360	173	0.97	0.08	45	0.2	0.1
M/NCf	200	—	—	—	—	—	0.4	2.9
	600	355	291	0.40	0.12	n. d.	0.3	0.1
M/NH_3	200	428	0	1.52	0.01	41	1.3	5.4
	600	480	128	1.56	0.05	43	0.1	0.1
E/NH_3	600	636	174	1.73	0.08	38	0.2	0
E/NH_3d	600	625	173	2.05	0.08	50	0.2	0

[a]S_{MP} denotes the specific micropore surface area derived from *t*-plot analysis. [b]V_P is the BJH cumulative desorption pore volume of pores in the maximum diameter range 1.7–300 nm. [c]V_{MP} denotes the specific micropore volume derived from *t*-plot analysis. [d]d_{max} is the graphically assessed pore size maximum of the pore size distribution derived from the adsorption branch.

3.1 Textural and structural properties

Table 2 lists the textural properties of all the aerogels. Pore size distributions and *t*-plots of the aerogels are given in the ESI. In general, the aerogels showed a type IV isotherm with a type H1 desorption hysteresis, according to IUPAC classification, and mesoporosity with graphically determined maxima of the pore size distribution in the range 20–50 nm. After calcination at 600 °C, the BET surface areas of the aerogels with 10wt% Fe_2O_3 prepared from TMOS were found to lie in the range 300–480 m^2 g^{-1} and the pore volume amounted to 0.72–1.56 cm^3 g^{-1}. The aerogels derived from TEOS and ammonia (E/NH_3, E/NH_3d) showed higher surface areas (around 630 m^2 g^{-1}) and pore volumes of 1.73–2.05 cm^3 g^{-1}. Among the aerogels with 10 wt% Fe_2O_3 calcined at 600 °C, the pore size distributions were narrowest for M/Tri and Md/NN; the higher size limit was set at 40 and 50 nm, respectively, with a maximum of the distribution at about 20 nm. The aerogels prepared using ammonium carbonate (M/NC) or ammonia (M/NH_3, E/NH_3, E/NH_3d) showed broader pore size distributions and the presence of macropores. Microporosity, as determined by the Harkins–Jura correlation, was more pronounced for the aerogels Md/NN, M/NN, M/Tri, M/NC and M/NCf. On the contrary, for the aerogels gelled by ammonia, the micropore share was much lower, amounting only to 3.5% of the pore volume and 25% of the surface area (Table 2). In general higher surface area with higher mesoporosity was achieved with aqueous ammonia as the gelation agent, whereas smaller mesopores and micropores were characteristic for the aerogels synthesized with *N,N*-diethylaniline and trihexylamine as gelation agents. Aqueous ammonium carbonate solutions gave a broad pore size distribution, ranging from micro- to macropores. Fast addition of the base in M/NCf increased the microporosity of the aerogel calcined at 600 °C. A more dilute prehydrolysis solution in Md/NN resulted in a narrower pore size distribution with smaller mesopores, up to 40 nm, and decreased pore volume in comparison to M/NN.

X-Ray diffraction analysis showed that after calcination at 600 °C, all aerogels with 10 wt% Fe_2O_3 were amorphous, irrespective of the sol–gel process applied. The absence of crystalline domains was confirmed by transmission electron microscopy combined with electron diffraction analysis. As already indicated by the textural properties (Table 2), the aerogels showed significant differences in morphology, which is illustrated by the transmission (Fig. 1) and scanning (Fig. 2) electron micrographs shown for samples M/NN and E/NH_3.

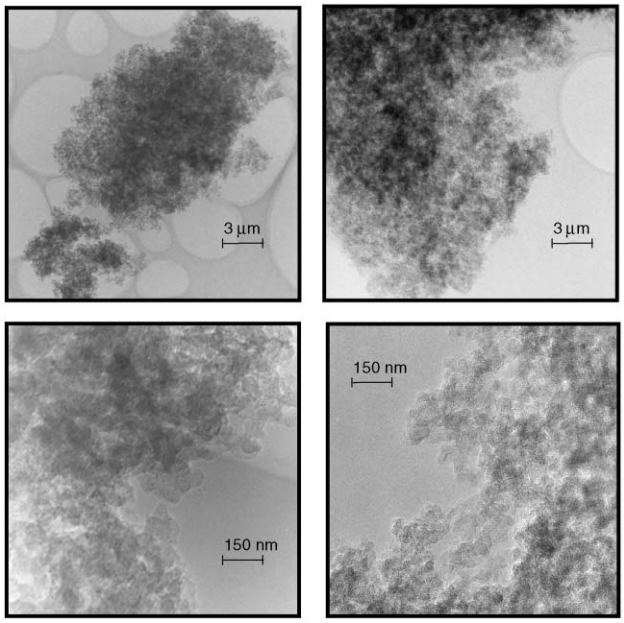

Fig. 1 Transmission electron micrographs of the aerogels M/NN (left) and E/NH_3 (right), calcined at 600 °C.

Note the pronounced flaky morphology of E/NH_3 compared to the more dense structure of M/NN.

Calcination of Md/NN at 900 instead of 600 °C (Md/NN900) led to shrinkage of the surface area at the expense of micropores (Table 2), whereas the pore volume was hardly influenced. The diffraction pattern of Md/NN900 showed a broad reflection at about 35° (Fig. 3), probably due to the formation of small γ-Fe_2O_3 or Fe_3O_4 crystallites, not distinguishable by XRD.

The iron content had a significant effect on the textural properties of the aerogels. The isotherms of 0/Md/NN (silica aerogel), 5/Md/NN and Md/NN showed type IV character with type H1 desorption hystereses, according to IUPAC classification. For 20/Md/NN, a type I isotherm with a type H4 hysteresis was observed, indicating the high microporosity of the material, which was confirmed by *t*-plot analysis. With increasing iron content, the BET surface area decreased from 740 (0/Md/NN) to 300–330 m^2 g^{-1} (Md/NN, 20/Md/NN; Table 2) accompanied by a decrease in the pore volume, as also shown in the pore size distribution plots (see ESI). The

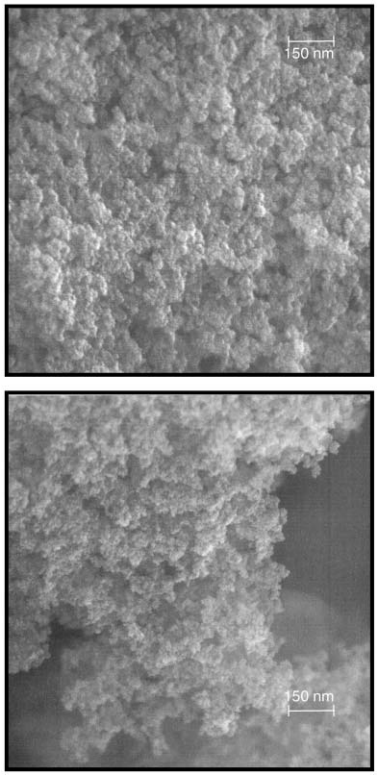

Fig. 2 Scanning electron micrographs of the aerogels M/NN (top) and E/NH_3 (bottom), calcined at 600 °C.

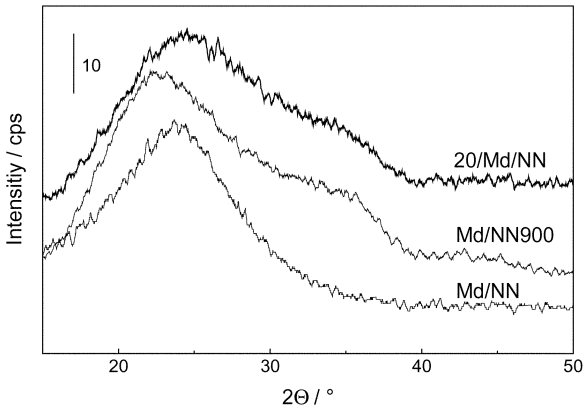

Fig. 3 XRD patterns of Md/NN, calcined at 600 and 900 °C (Md/NN900), and of 20/Md/NN.

maximum of the pore size distribution was around 40–45 nm for both 0/Md/NN and 5/Md/NN, considerably higher than for Md/NN (23 nm). XRD analysis of 20/Md/NN showed a broadening of the amorphous silica signal at 30–38°, which indicates the presence of small iron oxide clusters, analogously to Md/NN900 (Fig. 3).

3.2 Chemical properties

Chemical properties were investigated using AAS, elemental analysis, XPS, TPR, UV-Vis, EPR, transmission IR and DRIFT spectroscopy. The results are presented focussing on the effect of the N-base, iron content and calcination temperature.

Composition. The iron oxide content, determined by AAS, was 10 wt% for all aerogels with the nominal composition 10 wt% Fe_2O_3/SiO_2. For 20/Md/NN the measured iron content amounted to 17 wt% Fe_2O_3, instead of the nominal 20 wt%. Possibly loss of some iron occurred during supercritical extraction of the solvent. The nitrogen content of the aerogels after extraction did not reflect the amount of base used during the gelation step (Tables 1 and 2). However, a correlation between the strength of the base and the nitrogen content after extraction of the solvent seems to exist. For example, ammonia ($pK_a = 9.25$) is more strongly retained in the gel than *N,N*-diethylaniline ($pK_a = 6.6$),[40] whose content in the gel was about three times higher than that of ammonia. Besides enclosure in the bulk of the network or in pores, coordination to the surface seems to prevent ammonia from being extracted from the gel. Moreover, the bulkiness of the base may play a role in its ability to coordinate on the surface or in pores and could explain the low nitrogen content of the M/Tri gel (trihexylamine $pK_a = 8.53$).[41] Heat treatment at 200 °C significantly lowered the nitrogen content for the aerogels with the weak base *N,N*-diethylaniline and for M/NCf, whereas no noticeable change was observed for the aerogels produced with aqueous ammonia or trihexylamine and for M/NC. The use of a weak base and application of fast gelation therefore favours the desorption of the residues at low temperature.

After calcination in air at 600 °C, the aerogels showed negligible amounts of carbon and nitrogen (0.1–0.3 wt%). The elemental compositions of the surface regions were investigated using XPS. The surface oxygen, iron, silicon and nitrogen contents are listed in Table 3, together with the binding energy (BE) of the $Fe2p_{3/2}$ photoelectron measured for the calcined samples. Binding energies between 712.1–712.3 eV were found. The values were higher than the binding energies for bulk α-Fe_2O_3 (710.5;[42] 710.9;[43] 711.2 eV[44,45]) and Fe_3O_4 (710.5;[46] 711.2 eV[44]). This may indicate a strong interaction between iron and silica, in analogy with iron incorporated in Fe-ZSM-5 with a BE of 711.6 eV.[47] Nitrogen was only found in traces on

Table 3 Binding energy (BE) and surface composition of the calcined aerogels and of the differently reduced M/NH_3, as derived from XPS

Aerogel	BE $Fe2p_{3/2}$/eV	O content/at%	N content/at%	Fe content/at%	Si content/at%	Fe/Si[a]
M/NN	712.1	66.3	0.1	1	31.1	0.032
Md/NN	712.3	61.6	~0	0.9	32.0	0.028
Md/NN900	712.3	65.8	0.2	1.1	32.1	0.035
5/Md/NN	712.2	67.4	0.3	0.6	30.8	0.018
20/Md/NN	712.4	66.3	0.1	2.3	29.5	0.078
M/Tri	712.3	64.4	0.1	1.1	30.2	0.036
M/NH_3	712.1	67	0.1	1.1	29.9	0.033
M/NC	712.1	62.8	0.5	0.9	29.8	0.030
M/NCf	712.3	61.5	0.4	0.9	32.9	0.027
M/NH_3, TPR 420 °C[b]	712.2	66.1	0	1.1	31.5	0.035
M/NH_3, TPR 1100 °C[b]	706.5	63.7	0	1.1	34.0	0.032
E/NH_3	712.1	64.2	0.1	0.9	31.2	0.029
E/NH_3d	712.2	65.4	0.2	0.9	30.6	0.029

[a]Expected Fe/Si values from chemical composition: 5/Md/NN, 0.042; 20/Md/NN, 0.143; all other samples containing 10 wt% Fe_2O_3, 0.084. [b]After TPR to temperatures specified.

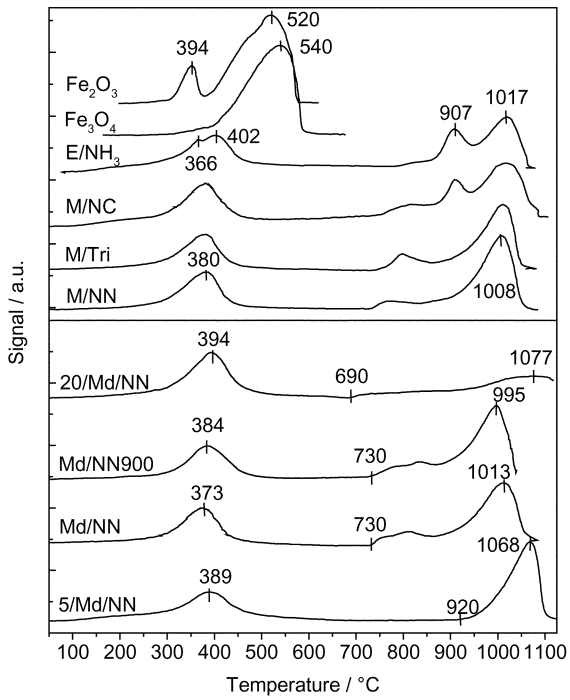

Fig. 4 TPR curves of selected aerogels after calcination at 600 °C. Top: aerogels prepared with different sol–gel conditions and the reference oxides Fe_2O_3 and Fe_3O_4. Bottom: curves for the aerogels with different iron loading or calcined at higher temperature.

the surfaces, in accordance with the elemental analyses. Comparison of the surface Fe/Si ratios with the values expected from the chemical composition revealed silicon enrichment in the surface region of all aerogels. Surface Fe/Si ratios reached only 30–50% of the theoretically expected values (Table 3).

Calcination at 900 °C (Md/NN900) increased the iron surface content slightly. The $Fe2p_{3/2}$ binding energy was 712.2–712.4 eV, independent of iron loading and calcination temperature. With higher iron loading, a satellite peak 720 eV increased in intensity. This satellite is characteristic for high spin Fe(III) species,[44,48] but seems to be independent of the type of oxide.[44]

After reduction at 420 °C (TPR), M/NH_3 did not show a significant shift in the $Fe2p_{3/2}$ binding energy. Likely, the surface is easily re-oxidized in air, as indicated by the slight darkening of the colour. After reduction at 1100 °C on the other hand, the $Fe2p_{3/2}$ binding energy corresponded to that of metallic iron,[43] in line with the results of the hydrogen consumption measurements and reflections for metallic iron detected by XRD.

Temperature programmed reduction. The TPR signals of some calcined aerogels are shown in Fig. 4 (top), and corresponding maximum temperatures of hydrogen consumption are listed in Table 4. The reduction onset was at about 280 °C, 35 °C higher than for Fe_3O_4, and 115 °C higher than for Fe_2O_3. The first maximum at about 385 °C was common to all samples and the hydrogen consumption corresponded to a change in the iron oxidation state of 0.8–1.1. Further reduction of the iron proceeded only at very high temperatures, in contrast to the pure Fe_2O_3 and Fe_3O_4 samples, where reduction was complete at 580 and 590 °C, respectively (Fig. 4). The high temperature reduction signals of M/NN, Md/NN and M/Tri were characterized by one strong signal at 1008–1013 °C and a small shoulder between 770 and 812 °C. For M/NC, M/NCf, M/NH_3, E/NH_3 and E/NH_3d, various reduction profiles were observed. Besides the maximum at around 1013–1020 °C, one or more signals at lower temperature appeared, which may indicate less homogenous iron incorporation in the silica matrix. After reduction up to 1100 °C, the samples were crystalline and showed X-ray diffraction patterns of quartz and Fe^0.

A slight narrowing of the high temperature signal was observed after calcination at 900 °C (compare Md/NN and Md/NN900 in Fig. 4, bottom) and the maximum was shifted from 1013 to 995 °C. The maximum of the first signal was shifted from 373 to 384 °C. The hydrogen consumption of the first and the second peak was similar for both samples (Table 4). The low iron load sample 5/Md/NN showed a broad signal at 389 °C, whereas further reduction only started at 920 °C. The consumed hydrogen in the second step corresponded to a change in oxidation state of 1.74, which may indicate that not all the iron was completely reduced at 1100 °C. The high iron load aerogel 20/Md/NN showed an intense reduction signal between 300 and 500 °C with an overall change in the oxidation state of iron of 1.6. About 30% of the iron is therefore already reduced completely at this temperature. Further reduction of the material started at 690 °C, at lower temperature than for the other aerogels, but was not complete at 1100 °C (Fig. 4 bottom, Table 4).

To sum up, TPR showed that the oxidation state of the iron was mainly 3+ for all aerogels after calcination. High temperature ($T > 700$ °C) was necessary for complete reduction. Higher iron loading (20/Md/NN) increased markedly the fraction of iron reduced below 500°C, whereas this was not the case for the sample calcined at high temperature (Md/NN900). The samples prepared with aqueous ammonia and ammonium carbonate solutions showed more complex reduction profiles, than the samples gelled with *N*,*N*-diethylaniline and trihexylamine, likely due to the presence of different iron oxide species.

Transmission IR-spectroscopy. Fig. 5 shows the IR spectra of aerogels with 0, 5, 10 and 17 wt% Fe_2O_3 (0/Md/NN, 5/Md/NN,

Table 4 Characteristic TPR features of the aerogels. Temperatures refer to the maxima of hydrogen consumption. Results for bulk Fe_2O_3 and Fe_3O_4 are given for comparson

Aerogel	1. Max./°C	2. Max./°C	3. Max./°C	4. Max./°C	ΔOx[a] (1. Max.)	ΔOx[a] (overall)
M/NN	381	770	—	1008	1.0	3.0
Md/NN	373	812	—	1013	1.0	2.9
Md/NN900	384	837	—	995	0.9	2.8
5/Md/NN	389	—	—	1068	0.9	2.6
20/Md/NN	394	690–1100	—	—	1.6	3.0
M/Tri	380	798	—	1010	0.9	2.9
M/NC	386	816	907	1017	0.9	2.9
M/NCf	395	813	928	1015	1.1	3.1
M/NH_3	378	697/803	—	1013	0.9	2.9
E/NH_3	366/402	—	909	1020	1.3	3.0
E/NH_3d	391	—	943	1020	1.2	2.9
Fe_3O_4	—	540	—	—	—	2.7
Fe_2O_3	351	507	—	—	—	3.0

[a]ΔOx: change in iron oxidation state as determined from H_2 consumption.

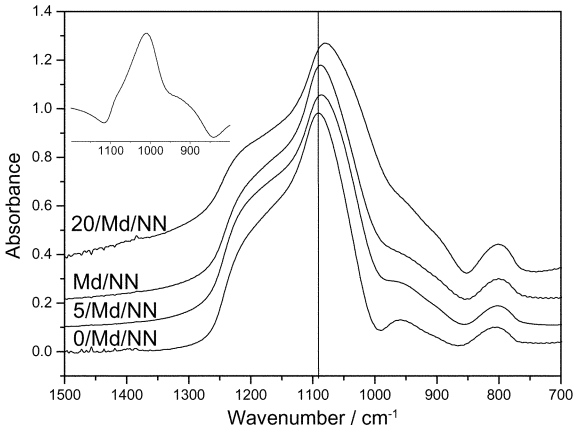

Fig. 5 IR transmission spectra of the pure silica aerogel (0/Md/NN) and Md/NN aerogels with different iron content, calcined at 600 °C. The inset shows the difference between the aerogel with 10% nominal Fe_2O_3 and the silica aerogel.

Md/NN, 20/Md/NN). With increasing iron content, the most intense band at around 1090 cm^{-1} broadened towards lower energy. As a consequence the Si–OH stretching vibration at 958 cm^{-1}, which was clearly separated from the strong band at 1090 cm^{-1} for the pure SiO_2 aerogel 0Md/NN, became less distinct. Also, the band at around 806 cm^{-1} was slightly shifted towards lower energy. Subtracting the spectrum of the pure SiO_2 aerogel from the Fe-containing aerogels resulted in a band at 1012 cm^{-1}, as shown in the inset of Fig. 5 for Md/NN.

IR spectroscopy has been used in the past to characterize Fe-silicalites[29,49] and is a convenient tool to investigate incorporation of iron in the silica framework. Silicalites as well as amorphous silica are characterized by bands in the 1300–1100 and 850–750 cm^{-1} regions associated with the Si–O stretching vibrations of the [SiO_4] unit. Locally, this unit has T_d symmetry, giving rise to vibrations of T_2 and A_1 representations. The former vibrations are IR active and associated with strong bands at 1300–1100 cm^{-1} (antisymmetric Si–O–Si vibrations). The latter give rise to weaker bands in the 850–750 cm^{-1} region (symmetric Si–O–Si vibrations). Incorporation of the heavy iron ion in the framework leads to a lowering of the local symmetry of the nearest neighbor [SiO_4] units to C_{3v} (O_3Si–O). This gives rise to a band at around 1010 cm^{-1}, *i.e.* at lower energy than the corresponding undisturbed [SiO_4] vibration.[3,29]

The described spectral features, based on the above discussion, indicate incorporation of iron into the SiO_2 framework. Also, the series shown in Fig. 5 suggests that the amount of incorporated iron increases with the nominal iron content. Among the different aerogels with 10% Fe_2O_3 content, the spectra showed no significant differences (not shown).

UV-Visible spectroscopy. Fig. 6 (bottom) shows the diffuse reflectance UV-Vis spectra of M/NH_3, E/NH_3, M/Tri, M/NN and Md/NN aerogels, diluted in $BaSO_4$, recorded under ambient conditions. The dominant charge transfer (CT) band around 255 nm is composed of several transitions between 220 and 300 nm, as becomes evident from the derivative spectra (not shown). Spin forbidden d–d transitions at higher wavelengths were partially masked by the long wavelength tail of the CT transitions. The first derivative spectra (Fig. 6 inset) give evidence of bands at around 350, 405 and 460–475 nm. Before calcination, the d-d transitions were observed at about 350, 405 and 450–460 nm (inset, Fig. 7).

Determination of the coordination environment is not unambiguous for d^5 ions, as the Tanabe–Sugano diagram is similar for tetrahedral and octahedral symmetry.[29,50] However, iron-modified molecular sieves and phosphates showed d–d bands at 370–392, 408–425, 433–454 and 471–481 nm, which were assigned to Fe^{3+} in a tetrahedral environment, in

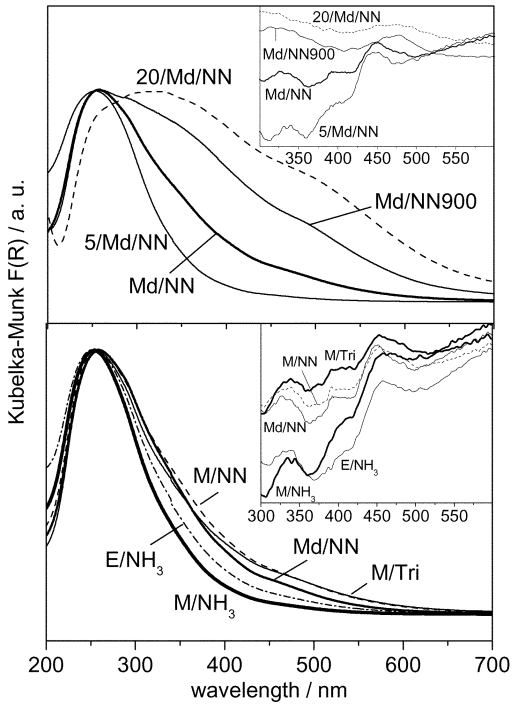

Fig. 6 UV-Vis spectra of aerogels prepared with different sol–gel conditions (bottom), calcined at 600 °C. Spectra of the aerogels with increasing iron loading, as well as of Md/NN calcined at 900 °C (top). Spectra were normalized to their maximum height for comparison. The inset shows the first derivatives of the spectra in the region 300–600 nm.

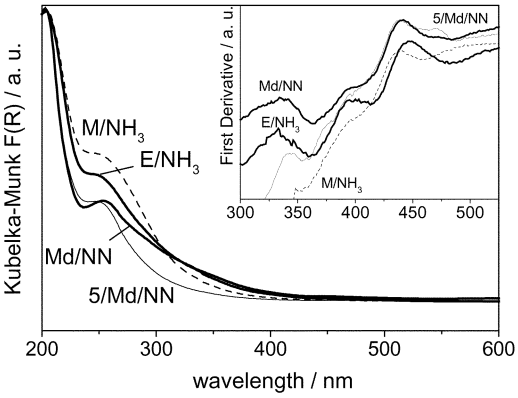

Fig. 7 UV-Vis spectra of the raw aerogels and after calcination at 600 °C. The inset shows the first derivative of the spectra in the region 300–525 nm.

agreement with the solution spectra and EPR and EXAFS measurements.[18,29,33,50–52] Also, a band at 357 nm was reported by Bordiga *et al.*[29] for tetrahedral Fe^{3+} in Fe-silicalite. Note that d–d transitions for octahedral Fe^{3+} are known to be about one order of magnitude weaker than for tetrahedral coordination. For octahedral Fe^{3+} in phosphate glasses,[50,51] d–d bands were observed at 415, 520 and 740 nm. Based on these reported UV spectra for Fe^{3+} in different environments, the d–d transitions in the spectra of the calcined aerogels with 10 wt% Fe_2O_3 (Fig. 6 bottom) and of the uncalcined aerogels (Fig. 7) are assigned to tetrahedrally coordinated Fe^{3+}. This assignment is also consistent with the observed low wavelength CT transitions of the calcined aerogels between 220 and 250 nm.[29,50,53–55] Comparison of the d–d band region in the spectra of the 10 wt% Fe_2O_3 loaded aerogels before and after calcination shows that the tetrahedrally coordinated Fe^{3+} (or at least part of it) resists calcination up to 600 °C. On the other hand, the CT bands markedly changed upon calcination (Fig. 6 and 7). The raw aerogel contains organic material,

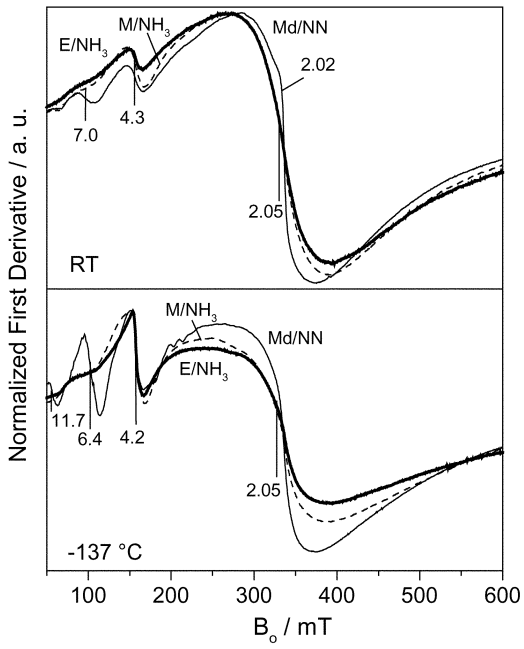

Fig. 8 EPR spectra of aerogels E/NH_3, M/NH_3 and Md/NN calcined at 600 °C, and evacuated to 0.01 mbar at RT. Measurements were performed at RT and −137 °C. Derivative spectra were normalized to the maximal positive value. *g* values of the main signals are marked in the plots.

which may be coordinated to the iron. Indeed, the type of ligand was found to influence the CT spectra much more than the ligand field spectra.[50]

The occurrence of high wavelength CT transitions is a strong indication for iron oxide clusters. Octahedral Fe^{3+} embedded in corundum showed a CT band at 278 nm, whereas a band at 333 nm was reported for small iron oxide clusters.[29,50] The absorption maximum for small clusters is expected to shift considerably with the size of the cluster due to quantum size effects.[56] Therefore, the presence of iron oxide nanoparticles is indicated by the tail of the CT bands extending into the visible, leading to a tan color for all calcined samples.

Fig. 6 (top) depicts the UV-Vis spectra of the aerogels with different iron loading and calcination temperature (Md/NN900). The absorption tail to longer wavelength, due to the presence of iron oxide agglomerates, is more pronounced with increasing iron content. Also the sample calcined at 900 °C showed a pronounced absorption in this range, in agreement with the XRD measurements (Fig. 3), which revealed the presence of small iron oxide crystallites. For the low iron load sample (5/Md/NN), the d–d bands due to tetrahedrally coordinated Fe^{3+} were clearly discernible, whereas for Md/NN900 and 20/Md/NN, broad absorptions at about 370 and 510 nm dominated the spectrum (inset of Fig. 6, top). The latter band is due to iron oxide agglomerates.[29] The low wavelength CT band was still pronounced in Md/NN900 indicating that part of the iron is still in tetrahedral sites after calcination at 900 °C.

Continuous wave electron paramagnetic resonance spectroscopy. EPR was widely used in the past to investigate the coordination of Fe^{3+} in ferroaluminosilicates,[30–33,55,57–60] Fe-silicalites,[29] Fe-aluminophosphates,[61,62] Fe-mesoporous silicas[54] and Fe^{3+} in glasses.[51,63,64]

Fig. 8 depicts the EPR spectra of the aerogels E/NH_3, M/NH_3 and Md/NN, calcined at 600 °C, after evacuation to 0.01 mbar at room temperature. Table 5 lists the position and also the widths of the main signals. Spectra recorded at room temperature showed main features at $g = 4.3$ and 2.05. At low field, a second component at about $g = 7.0$ occurred (Fig. 8), which was most clearly discerned for Md/NN. The signal at 4.3 has been reported for both octahedrally and tetrahedrally coordinated Fe^{3+} with rhombic distortion of the site.[29,33,51,55,65] The signals at lower field were assigned to less distorted iron sites in tetrahedral coordination.[29,33,61] The broad asymmetric signal at 2.05 is composed of two components at about $g = 2.3$–2.5 and 2.00.[29,33,55,58,59] The signal at 2.3 has been assigned quite unanimously to small iron oxide particles. It showed increasing relative intensity in the series Md/NN < M/NH_3 < E/NH_3. The signal at 2.00 can be assigned to Fe^{3+} in a symmetric environment (T_h or O_h), which is consistent both with framework and extraframework Fe^{3+}.[33] Bordiga *et al.*[29] assigned a signal at 2.0 to the framework iron brought into perfect tetrahedral coordination by the adsorption of water. Indeed, degassing led to a decrease of this band due to dehydration, as demonstrated in Fig. 9. Therefore, we assign part of the signal at 2.0 to framework Fe^{3+} coordinated by water in a asymmetrical tetrahedral environment, in agreement with the UV-Vis results.

Upon cooling to −137 °C (Fig. 8, bottom), an increase in the low field signals relative to the signals between 2.4 and 2.0 was observed. The signals due to isolated iron species at $g = 2.0$ may broaden, as some thermal movement is suppressed, whereas mutual magnetic interaction of aggregated Fe^{3+} leads to a *g*-shift and line width increase of the signal at 2.3 upon cooling.[29,33,58] At −137 °C, a strong signal at 6.4, associated with iron in a distorted tetrahedral environment[33,61] was observed for Md/NN, together with a smaller one at 11.7. Furthermore, the weak but sharp signal at $g = 2.02$ (ΔB = 9 mT) observed at room temperature decreased upon cooling. A signal at $g = 2.0$ with similar shape and behaviour upon cooling due to superparamagnetic relaxation was also found by Gazeau *et al.*[66] and Wajnberg *et al.*[67] for non-crystalline

Table 5 Positions and line widths (in parentheses) of the main EPR signals in the spectra measured at room temperature (RT) and −137 °C (LT). Line widths were computed as the difference between the maximum and minimum of the derivative spectra

Aerogel	Pressure/mbar	*g* (ΔB/mT) low field, RT	*g* (ΔB/mT) high field, RT	*g* (ΔB/mT) low field, LT	*g* (ΔB/mT) high field, LT
Md/NN	—	4.47 (20)	2.06 (82)	4.37 (18)	2.06 (93)
	10	4.44 (18)	2.06 (83)	4.37 (17)	2.08 (88)
	0.01	4.32 (10)	2.05 (87)	4.24 (12)	2.07 (95)
		6.95 (19)	2.02 (9)	6.45 (19)	
				11.74 (12)	
Md/NN900	0.01	—	2.007 (8.4)	4.29 (3)	2.005 (23)
5/Md/NN	0.01	4.30 (16)	2.10 (100)	4.27 (16)	2.10 (92)
20/Md/NN	0.01	—	2.007 (12)	4.31 (6)	2.005 (24)
M/NH_3	0.01	4.32 (21)	2.06 (119)	4.25 (17)	2.04 (109)
E/NH_3	—	4.42 (15)	2.04 (99)	4.37 (18)	2.06 (80)
	10	4.39 (16)	2.03 (103)	4.35 (17)	2.07 (94)
	0.01	4.29 (15)	2.04 (122)	4.23 (13)	2.05 (122)
	1×10^{-6}	4.20 (14)	2.04 (138)	4.21 (13)	2.05 (122)

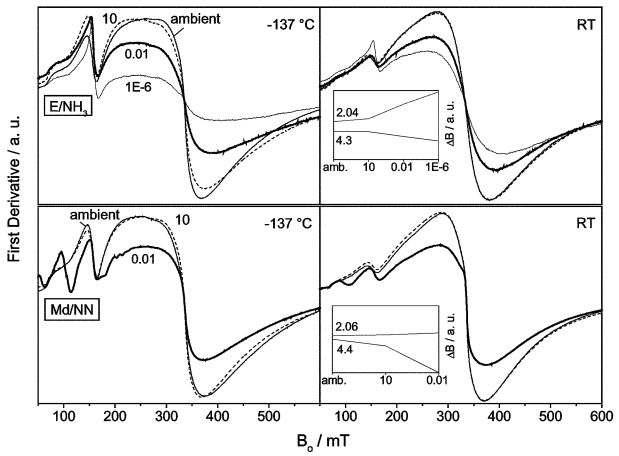

Fig. 9 EPR spectra of the aerogels Md/NN (bottom) and E/NH_3 (top), calcined at 600 °C. Samples were evacuated to decreasing pressures, marked in mbar in the plots. Measurements were performed at RT (right) as well as −137 °C (left). The inset shows the change in the peak linewidth ΔH with evacuation for the measurements at RT (scalings are different for the 4.4–4.3 and 2.06–2.04 lines).

maghemite and magnetite nanoparticles. Magnetic anisotropy was likely due to a strong interaction with the support. Ferromagnetic iron oxide particles with $g = 2.00$ were also characterized by Bordiga *et al.*[29] The signal at 2.02 for Md/NN may therefore be assigned to an additional species; tiny, magnetically anisotropic iron oxide (maghemite) clusters, strongly interacting with the silica matrix.

Fig. 9 shows that degassing also leads to an increase in the signals at $g = 10$–4.3 and a sharpening of the signal at $g = 4.3$ associated with distorted tetrahedral or rhombic sites. A sharpening of the $g = 4.3$ signal and a broadening of the $g = 2$ signal is indeed predicted with increasing distortion of the environment (increasing E/D) of framework iron,[33,61] here likely caused by dehydration. However, the formation of new distorted Fe-O-Si sites upon dehydration of extraframework iron hydroxide was suggested by Goldfarb *et al.*[33] and cannot be excluded.

EPR spectra of aerogels with different iron loading are shown in Fig. 10. Changing the iron oxide content from 5 to 10 wt% Fe_2O_3 showed a clear increase of the signal associated with the distorted tetrahedral sites at $g = 6.4$ in the spectra measured at −137°C. Increasing the calcination temperature up to 900 °C led to a dramatic change in the spectra. The signal at $g = 2.02$ increased and shifted to $g = 2.007$, maintaining the same line width ($\Delta B = 8.4$ mT) as in the spectrum measured at room temperature. Also, a low field signal at $g = 3.91$ was observed. Both peaks were reduced in intensity in the spectra measured at −137 °C and may be tentatively assigned to the same superparamagnetic Fe–O–Fe species. In the sample with 17 wt% Fe_2O_3 (20/Md/NN), these signals were also detected. Additionally, for this sample, a broad peak at about $g = 2.3$ due to iron oxide clusters was observed. A small signal at $g = 4.3$ in the samples with 17 wt% Fe_2O_3 and that calcined at 900 °C indicated that some iron is still incorporated in the silica matrix.

In conclusion, EPR clearly shows the existence of different iron species. In addition to isolated, tetrahedrally coordinated iron and iron oxide clusters, superparamagnetic iron oxide clusters were observed. Their abundance increased with the iron loading.

Hydroxyl groups studied by DRIFTS. DRIFT spectra of the hydroxyl region of some of the mixed oxide aerogels, and of the silica aerogel treated *in situ* at 300 °C are depicted in Fig. 11. At this temperature, dehydration of a silica surface is supposed to be complete, whereas dehydroxylation of the isolated hydroxyls does not occur.[37] The aerogels showed distinctly different

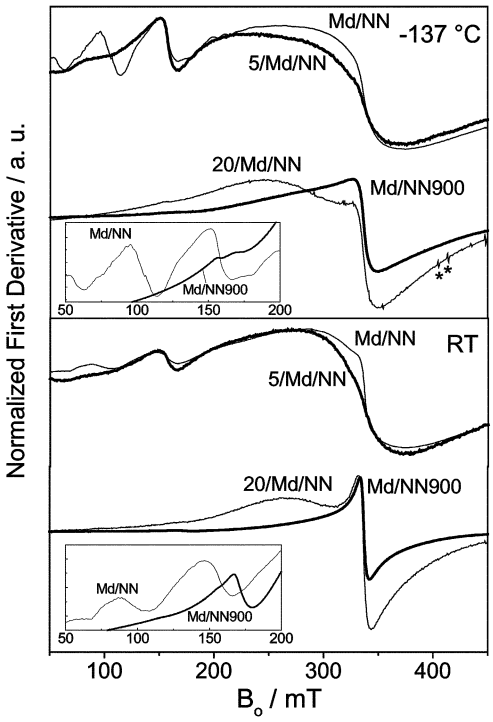

Fig. 10 EPR spectra of the aerogels with increasing iron loading, calcined at 600 °C, and Md/NN900 calcined at 900 °C. The derivative spectra were normalized to the maximum positive values. Insets show the magnified 50–200 mT region for Md/NN and Md/NN900. Asterisks indicate gaseous O_2 in low concentration.[73]

spectra depending on the sol–gel method applied. In general, the ν(OH) vibrations were spread over a much broader frequency range compared to the corresponding silica aerogel, where the main vibration was that due to isolated Si–OH groups at 3747 cm^{-1}. Only a few vicinal interacting silanols were detected in the region 3730–3520 cm^{-1} on the dehydrated silica.[37]

Among the mixed oxide aerogels, the samples with the highest amount of hydroxyls were those gelled by *N,N*-diethylaniline, M/NN and Md/NN, followed by M/Tri, M/NC, and M/NH_3. E/NH_3 and E/NH_3d showed much less

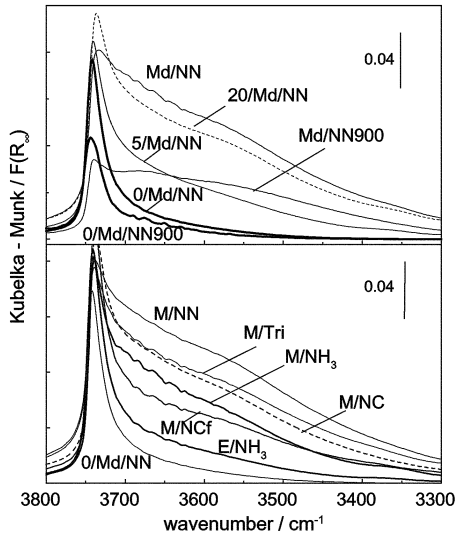

Fig. 11 DRIFT spectra of the calcined aerogels, dried *in situ* in air at 300 °C. Top: aerogels with different iron loading prepared with *N,N*-diethylaniline as gelation agent. Bottom: aerogels containing 10% nominal Fe_2O_3 prepared with different bases used as gelation agent. In both figures, the spectrum of pure silica aerogel 0/Md/NN is given as a reference.

hydroxyl groups. Bordiga *et al.*[29] as well as Datka and Abramowicz[68] studied the hydroxyl region of ferrisilicalites under different conditions. Under heat treatment in vacuum at 300-400 °C, a sharp band at 3630 cm^{-1} appeared, which was assigned to bridged Fe(OH)Si in analogy to the more acidic Al(OH)Si moiety. The band was less pronounced after treatment in air. Similarly, we ascribe the broad band between 3700 and 3400 cm^{-1} to Fe(OH)Si entities. The broadness of the band indicates a large distribution of different Fe(OH)Si groups. Also, internal H-bonded silanols (hydroxyl nests) were reported to occur in the region 3660–3450 cm^{-1},[29,37] which were found to disappear during treatment of amorphous silica at temperature higher than 500 °C.[37] We have shown elsewhere[69] that these hydroxyls exhibit Brønsted acidity upon adsorption of ammonia. The amorphous character and the high iron content of the aerogels is likely the reason for the much broader inhomogeneous line widths of the Fe(OH)Si band as compared to zeolites.

Fig. 11 (top) shows the DRIFT spectra of the aerogels with different iron loading. The amount of acidic hydroxyl groups in the region 3700–3400 cm^{-1} increased in the series 5/Md/NN < 20/Md/NN < Md/NN. The aerogel 0/Md/NN is shown for comparison. Md/NN900 should be compared with the corresponding silica aerogel, 0/Md/NN900, as treatment at higher temperature markedly reduced the overall amount of hydroxyl groups due to irreversible dehydroxylation. The amount of acidic hydroxyl groups on Md/NN900 was still remarkable after high temperature treatment. A broad but distinct vibration at 3680 cm^{-1} could be discerned, which occurs very close to that found for Fe(OH)Si groups on ferrisilicalites.[29,68]

4 Discussion

The results presented here demonstrate that amorphous iron oxide–silica aerogels with high surface area can be prepared by the solution-sol–gel method. The properties of the aerogels, particularly their texture and the state of the iron can be influenced by the synthesis procedure. This seems particularly attractive for their potential use as catalysts. In the following, we focus on the influence of various synthesis parameters on the properties of the aerogels. In particular we discuss the effect of the N-base as gelling agent, the water content, the iron content and the temperature treatment of the aerogel.

The aerogels calcined in air at 600 °C showed meso- to micropores, depending on the sol–gel conditions applied. The morphological properties were largely determined by the gelation and ageing process, which are strongly influenced by the base type and water content of the sol (Table 2). High water content and basic conditions enhance the dissolution rate of the polymerized silica. For aqueous solutions in the intermediate pH range (3–8) the condensation rate was also reported to increase. Phenomena like Ostwald ripening and coarsening lead to stiffening of the gel and a decrease in the number of micropores.[3] Indeed, we observe high surface area and mesoporosity for the aerogels gelled by aqueous ammonia solutions (M/NH_3, E/NH_3, E/NH_3d). This is also reflected by the flaky morphology of aerogel E/NH_3, as is obvious from the TEM picture (Fig. 1). The amount of alcohol was higher for E/NH_3d than for E/NH_3, and a broader pore size distribution was observed. In M/NH_3, the high dilution of the sol by alcohol probably hindered the processes necessary for the formation of a stiff gel, leading to lower surface area. In comparison to these aerogels, those produced by the ammonium carbonate–water solution (M/NC, M/NCf) showed lower pore volume and mesoporosity. The gelation was forced by a solution with 6 times more water (H_2O : Si = 12.8) and higher basicity. These conditions are known to strongly enhance the dissolution rate of the silica and to lead to the formation of compact particles.[3] Gelation speed had a pronounced effect on the textural properties. For the fast gelled M/NCf aerogel, the pore volume of the calcined aerogel was half of the value obtained for M/NC, gelled by slow base addition, and microporosity was enhanced.

The silicon enrichment on the surface, as revealed by XPS measurements, indicates that condensation involving iron is faster than condensation of silica. It is known that Fe(OH)Si groups are more acidic than silanol groups and that more highly acidic OH accelerates the base-catalyzed condensation of silica.[3] Silica–iron complexes may therefore condense faster than polymerized silica, hence leading to iron enrichment in the core of the gel particles. The several characterisation methods applied to the calcined aerogels clearly show the co-existence of different iron species. Part of the iron is incorporated in the SiO_2 framework in tetrahedral environments, as shown by UV-Vis, IR and EPR spectroscopy. EPR also shows the presence of different tetrahedrally coordinated iron, ranging from symmetric to distorted tetrahedral environments. DRIFTS spectra additionally demonstrate the presence of Fe(OH)Si groups on the aerogels, which are associated with framework iron.[29] On the other hand, amorphous iron oxide clusters are present, as shown by UV-Vis and EPR, with varying sizes, phases and magnetic properties. EPR shows the existence of different iron oxide particles, characterized by signals at $g = 2.3$ and 2.02 (superparamagnetic particles). NO adsorption studies by DRIFTS further support the presence of different low coordinated iron species, and these will be presented elsewhere.[69] NO bound to low coordinate iron could be discerned parallel to a broad band due to NO on higher coordinated iron species. These bands were associated with iron incorporated in the amorphous SiO_2 and with iron oxide clusters, respectively.[70] Finally, small iron oxide crystallites are present in high iron content aerogels (17 wt% Fe_2O_3) and aerogels calcined at high temperature (900 °C), as indicated by XRD and confirmed by EPR.

All aerogels with 10 wt% Fe_2O_3, calcined at 600 °C, contain iron incorporated in the framework and iron oxide clusters, as determined by UV-Vis and EPR. However, the iron clusters or agglomerates are very small, as demonstrated by electron microscopy (TEM, SEM), and amorphous, since no indication of long range order was found by the diffraction techniques (XRD, selected area electron diffraction analysis). This claim is furthermore supported by the homogeneous distribution of the iron within the material, observed by energy dispersive X-ray emission analysis (EDX). Strong interaction of all iron species with the silica occurs, as TPR of the aerogels showed reduction profiles completely different from those of Fe_2O_3 and Fe_3O_4, and reduction to metallic iron only started above 700 °C. Bordiga *et al.*,[29] as well as Brabec *et al.*[71] associated high temperature reduction of Fe^{2+} to iron incorporated in the framework. However, iron oxide nanoclusters were also reported to resist reduction up to 800 °C.[24]

As indicated by DRIFTS, the amount of Fe(OH)Si groups, which determines the Brønsted acidity of the aerogels, is strongly affected by the N-base. The aerogels prepared using *N,N*-diethylaniline and trihexylamine showed considerably more Fe(OH)Si groups than those prepared with ammonia and ammonium carbonate. On the other hand, EPR showed a larger signal associated with small iron oxide particles for the samples prepared with ammonia (M/NH_3, E/NH_3) than for that prepared with *N,N*-diethylaniline (Md/NN). Concomitantly, the signals due to tetrahedrally coordinated iron were more pronounced on the latter sample. This indicates that use of aqueous ammonia or ammonium carbonate solution as the gelation agent favours formation of small iron oxide particles, whereas the use of *N,N*-diethylaniline and trihexylamine is favourable for incorporation of the iron into the SiO_2 framework of the aerogels. The speed with which the base was added was observed to influence the textural properties of the aerogel, whereas it probably does not strongly affect the

coordination of the iron in the aerogel, as seen by comparing the TPR and DRIFTS results for the M/NC and M/NCf. Furthermore, the presence of low polymerized silica is favourable to the incorporation of the iron in the framework,[36] as more acidic Si–OH groups are present in polymers than in monomers. Raman spectra (not shown) of the silica solutions recorded prior to addition of the iron precursor showed that weakly branched polymers had formed, associated with the intense SiO_4 stretching vibrations ascribed to linear $Si(OH)_n$-$(OCH_3)_{2-n}$–O–Si and to Si(OH)–$(O–Si)_2$ groups.[3]

High amounts of nitrogen were found to be present in the gel after extraction of the solvent with supercritical CO_2, due to the presence of base. Strong coordination of the base to the iron was proposed to explain the retention of the ammonia during treatment in air at 200 °C. *N,N*-diethylaniline and trihexylamine were more easily desorbed, probably as coordination to iron is reduced by the lower basicity and the bulkiness of these bases. The interaction of the iron with the base may be an important factor for the stability of the state of the iron ion. As described above, dissolution and recondensation occur in the gels with high pH and water content. The iron incorporated in the silica may be favourably redissolved if strong coordination to the base or complexation is possible. Also, during calcination this may help the extraction of the iron from framework sites and thus favour the formation of iron oxide particles under strongly oxidising conditions.

With increasing iron loading, both the surface area and the pore volume decreased. For sample 20/Md/NN with 17 wt% Fe_2O_3, XRD indicated formation of small iron oxide crystallites. Also, based on the UV-Vis spectra, one can conclude that the amount of iron present as iron oxide clusters, giving rise to the absorption tail into the visible, increases with loading, most significantly when going from 10 to 17% loading (Fig. 6). For the highly loaded sample, EPR shows an intense signal at $g = 2.3$, assigned to iron oxide particles. Additionally, the formation of superparamagnetic particles of amorphous iron oxide nanoclusters is found. During TPR, part of the iron was completely reduced at low temperature (< 500 °C), whereas about 70% of the iron was reduced above 700 °C, showing strong interaction with the silica. This indicates that upon increasing the loading to 17 wt% or above, the iron starts to form larger iron oxide aggregates. This is also supported by the relative surface iron content of the aerogels, as determined by XPS, which was more than two times higher for 20/Md/NN than for 10/Md/NN (Table 3). On the other hand, the infrared spectra of the lattice vibrations (Fig. 5) show that incorporation of iron into the SiO_2 framework increases with iron loading. Also, NO adsorption studies[69] and the DRIFT spectra of the hydroxyl groups strongly indicate that part of the iron is still incorporated in the silica for the highly loaded aerogel. Comparing the samples with increasing iron content (5, 10, 17 wt% Fe_2O_3), it becomes evident that the aerogel with 10 wt% contains the highest amount of incorporated iron ions. This is also consistent with the EPR data, which show a clear increase in the tetrahedral sites between 5 and 10% loading and significantly more iron within iron oxide clusters for the sample with 17% loading as compared to the lower iron load samples. Concomitantly, a decrease in surface area and mesoporosity is observed in the series 0/Md/NN > 5/Md/NN > 10/Md/NN > 20/Md/NN. It can therefore be concluded that the ratio of iron incorporated in the SiO_2 framework to that within clusters decreases with increasing loading, most significantly above 10%.

It is known that calcination favours migration of framework iron to extraframework sites.[29] For Fe-silicalites, Bordiga *et al.*[29] concluded that part (about 20%) of the iron moves from framework to extraframework sites during calcination at 500 °C, whereas after calcination at 700 °C, this process was almost complete. The results presented here show that after calcination of the aerogels at 600 °C, part of the iron is still incorporated within the framework. However, calcination at 900 °C had a significant effect on the aerogel's properties. First of all, high temperature calcination led to a significant decrease in surface area. In particular, the contribution of the micropores decreased dramatically. This was accompanied by the appearance of a weak reflection in the X-ray diffraction pattern due to γ-Fe_2O_3 or Fe_3O_4 crystallites. In several studies, the formation of γ-Fe_2O_3 was reported for Fe_2O_3–SiO_2 xerogels.[7–10,72] Also, UV-Vis showed an increase in the signals due to iron oxide clusters or aggregates upon high temperature calcination, whereas the amount of Fe(OH)Si groups, as determined by DRIFTS, decreased significantly. Migration of framework iron to extraframework sites is supported by the increase of the surface iron content after high temperature calcination, as determined by XPS. Interestingly, calcination at high temperature led to a strong signal in the EPR spectra, assigned to superparamagnetic iron oxide nanoclusters, observed to some extent also in 20/Md/NN. Formation of superparamagnetic particles in iron oxide–silica mixed oxides was also reported by Cannas *et al.*[7]

5 Conclusions

Iron–silicon mixed oxide aerogels with properties suitable for use in catalysis have been synthesized using a sol–gel process combined with subsequent supercritical extraction. Major sol–gel parameters varied were: type of N-base used as gelation agent, concentration of iron precursor, and water content. All synthesized aerogels were mostly amorphous with prominent mesoporosity. The iron content and calcination temperature were identified as important parameters for iron dispersion. UV-Vis and EPR spectroscopy revealed that the aerogels contained different iron species, ranging from tetrahedrally coordinated iron atoms incorporated in the silica matrix to iron oxide nanoclusters. The reduction behaviour of these species is strongly different, as indicated by their corresponding reduction profiles. High iron concentration and high calcination temperature favour the formation of iron oxide nanoclusters. The type of N-base used as the gelation agent mainly affects the Brønsted acidity and the textural properties of the resulting aerogels. Textural properties are also affected by the water content of the gel. The novel iron oxide–silica aerogels show interesting potential as catalysts for environmentally important reactions, as reported elsewhere.[69]

Acknowledgement

The authors thank Dr Frank Krumeich for TEM measurements, Dr M. Maciejewski for XRD measurements, and Dr M. Müller for the SEM measurements. Financial support by the ETH-Jubiläumsfonds (TEMA-Project) is gratefully acknowledged.

References

1 J. Fricke, *Spektrum der Wissenschaft*, 1988, **Juli**, 60.
2 N. Hüsing and U. Schubert, *Angew. Chem., Int. Ed.*, 1998, **37**, 22.
3 C. J. Brinker and G. W. Scherer, *Sol-Gel Science, the Physics and Chemistry of Sol-Gel Processing*, Academic Press, San Diego, CA, 1990.
4 M. Schneider and A. Baiker, *Catal. Rev. Sci. Eng.*, 1995, **37**, 515.
5 G. M. Pajonk, *Appl. Catal.*, 1991, **72**, 217.
6 E. I. Ko, J.-P. Chen and J. G. Weissmann, *J. Catal.*, 1987, **105**, 511.
7 C. Cannas, G. Concas, D. Gatteschi, A. Falqui, A. Musinu, G. Piccalunga, C. Sangregorio and G. Spano, *Phys. Chem. Chem. Phys.*, 2001, **3**, 832.
8 G. Ennas, A. Musinu, G. Piccaluga, D. Zedda, D. Gatteschi, C. Sangregorio, J. L. Stanger, G. Concas and G. Spano, *Chem. Mater.*, 1998, **10**, 495.
9 F. del Monte, M. P. Morales, D. Levy, A. Fernandez, M. Ocana,

A. Roig, E. Molins, K. O'Grady and C. J. Serna, *Langmuir*, 1997, **13**, 3627.
10 D. Niznansky, N. Viart and J. L. Rehspringer, *J. Sol-Gel Sci. Technol.*, 1997, **8**, 615.
11 K. Kearby, S. S. Kistler and S. Swann, *Ind. Eng. Chem.*, 1938, **30**, 1082.
12 D. Bianchi, H. Batis-Landoulsi, C. O. Bennett, G. M. Pajonk, P. Vergnon and S. J. Teichner, *Bull. Soc. Chim. Fr.*, 1981, 345.
13 L. Casas, A. Roig, E. Rodriguez, E. Molins, J. Tejada and J. Sort, *J. Non-Cryst. Solids*, 2001, **285**, 37.
14 M. Soufyani, D. Bourret, A. Sivade and R. Sempere, *J. Non-Cryst. Solids*, 1992, **145**(1–3), 60.
15 C. T. Wang and R. J. Willey, *J. Non-Cryst. Solids*, 1998, **225**, 173.
16 R. J. Willey, H. Lai and J. B. Peri, *J. Catal.*, 1991, **130**, 319.
17 R. J. Willey, S. A. Oliver, G. Olivieri and G. Busca, *J. Mater. Res.*, 1993, **8**(6), 1418.
18 P. Ratnasamy and R. Kumar, *Catal. Today*, 1991, **9**(4), 329.
19 T. Seiyama, T. Arakawa, T. Matsuda, Y. Takita and N. Yamazoe, *J. Catal.*, 1977, **48**, 1.
20 A.-Z. Ma and W. Grünert, *Chem. Commun.*, 1999, 71.
21 R. Q. Long and R. T. Yang, *J. Catal.*, 2000, **194**, 80.
22 H. Y. Chen, T. Voskoboinikov and W. M. H. Sachtler, *J. Catal.*, 1998, **180**, 171.
23 K. Hadjiivanov, H. Knözinger, B. Tsyntarski and L. Dimitrov, *Catal. Lett.*, 1999, **62**, 35.
24 R. Joyner and M. Stockenhuber, *J. Phys. Chem. B*, 1999, **103**, 5963.
25 L. J. Lobree, I. C. Hwang, J. A. Reimer and A. T. Bell, *Catal. Lett.*, 1999, **63**(3–4), 233.
26 J. O. Petunchi and W. K. Hall, *J. Catal.*, 1982, **129**, 202.
27 Y.-F. Chang, J. G. McCarty and Y. L. Zhang, *Catal. Lett.*, 1995, **34**, 163.
28 P. M. Marturano, L. Drozdová, A. Kogelbauer and R. Prins, *J. Catal.*, 2000, **191**, 460.
29 S. Bordiga, R. Buzzoni, F. Geobaldo, C. Lamberti, E. Giamello, A. Zecchina, G. Leofanti, G. Petrini, G. Tozzola and G. Vlaic, *J. Catal.*, 1996, **158**, 486.
30 P. Fejes, J. B. Nagy, K. Lazar and J. Halasz, *Appl. Catal., A*, 2000, **190**, 117.
31 A. Ribera, I. Arends, S. de Vries, J. Perez-Ramirez and R. A. Sheldon, *J. Catal.*, 2000, **195**, 287.
32 A. V. Kucherov, C. N. Montreuil, T. N. Kucherova and M. Shelef, *Catal. Lett.*, 1998, **56**, 173.
33 D. Goldfarb, M. Bernardo, K. G. Strohmaier, D. E. W. Vaughan and H. Thomann, *J. Am. Chem. Soc.*, 1994, **116**, 6344.
34 F. Blanchard, B. Pommier, J. P. Reymond and S. J. Teichner, *Stud. Surf. Sci. Catal.*, 1983, **16**, 395.
35 R. J. Meyer, E. H. E. Pietsch and M. Becke-Goehring, in *Gmelin Handbook of Inorganic and Organometallic Chemistry*, Springer, Berlin, 1975.
36 R. A. Porter and W. J. Weber, *J. Inorg. Nucl. Chem.*, 1971, **33**, 2443.
37 E. F. Vansant, P. Van Der Voort and K. C. Vrancken, *Stud. Surf. Sci. Catal.*, 1995, **93**, 59.
38 D. M. Monti and A. Baiker, *J. Catal.*, 1983, **83**, 323.
39 C. D. Wagner, L. E. Davis, M. V. Zeller, J. A. Taylor, R. M. Raymond and L. H. Gale, *Surf. Interface Anal.*, 1981, **3**, 211.
40 *CRC Handbook of Chemistry and Physics*, ed. D. R. Lide, CRC Press, London, 1993.
41 A. K. Borrows, *J. Chem. Soc.*, 1947, 200.
42 K. Hirokawa and M. Oku, *Talanta*, 1979, **26**, 855.
43 D. Briggs and M. P. Seah, *Practical Surface Analysis*, Wiley, New York, 1982.
44 C. R. Brundle, T. J. Chuang and K. Wandelt, *Surf. Sci.*, 1977, **68**, 459.
45 G. C. Allen, S. J. Harris and J. A. Jutson, *Appl. Surf. Sci.*, 1989, **37**, 111.
46 T. J. Udovic and J. A. Dumesic, *J. Catal.*, 1984, **89**, 303.
47 R. B. Borade, A. Adnot and S. Kaliaguine, *Zeolites*, 1991, **11**, 710.
48 M. Oku and K. Hirokawa, *J. Electron Spectrosc.*, 1976, **8**, 475.
49 R. Kumar, A. Thangaraj, R. N. Bhat and P. Ratnasamy, *Zeolites*, 1990, **10**, 85.
50 G. Lehmann, *Z. Phys. Chem., Neue Folge*, 1970, **72**, 279.
51 C. R. Kurkjian and E. A. Sigety, *Phys. Chem. Glasses*, 1968, **9**(3), 73.
52 B. Echached, A. Moen, D. Nicholson and L. Bonneviot, *Chem. Mater.*, 1997, **9**, 1716.
53 B. N. Figgis, *Introduction to ligand fields*, Wiley, New York, 1986.
54 A. Tuel, I. Arcon and J. M. M. Millet, *J. Chem. Soc., Faraday Trans.*, 1998, **94**, 3501.
55 D. H. Lin, G. Coudurier and J. C. Vedrine, *Zeolites: Facts, Figures, Future*, ed. P. A. Jacobs and R. A. van Santen, Elsevier, Amsterdam, 1989.
56 T. Abe, Y. Tachibana, T. Uematsu and M. Iwamoto, *J. Chem. Soc., Chem. Commun.*, 1995, 1617.
57 A. M. Volodin, V. I. Sobolev and G. M. Zhidomirov, *Kinet. Catal.*, 1998, **39**, 775.
58 H. Y. Chen, E. M. El-Malki, X. Wang, R. A. van Santen and W. M. H. Sachtler, *J. Mol. Catal. A: Chem.*, 2000, **162**, 159.
59 E. M. El-Malki, R. A. van Santen and W. M. H. Sachtler, *J. Catal.*, 2000, **196**, 212.
60 E. M. El-Malki, R. A. van Santen and W. M. H. Sachtler, *J. Phys. Chem. B*, 1999, **103**, 4611.
61 D. Arieli, D. E. W. Vaughan, K. G. Strohmeier, H. Thomann, M. Bernardo and D. Goldfarb, *Magn. Reson. Chem.*, 1999, **37**, 43.
62 A. Brückner, U. Lohse and H. Mehner, *Microporous Mesoporous Mater.*, 1998, **20**, 207.
63 T. Castner, Jr., G. S. Newell, W. C. Holton and C. P. Slichter, *J. Chem. Phys.*, 1960, **32**(3), 668.
64 M. Nofz, R. Stosser, B. Unger and W. Herrmann, *J. Non-Cryst. Solids*, 1992, **149**, 62.
65 A. F. Karimova, *Teor. Eksp. Khim.*, 1981, **17**(2), 268.
66 F. Gazeau, V. Shilov, J. C. Bacri, E. Dubois, F. Gendron, R. Perzynski, Y. L. Raikher and V. I. Stepanov, *J. Magn. Magn. Mater.*, 1999, **202**, 535.
67 E. Wajnberg, D. Acosta-Avalos, L. J. El-Jaick, L. Abraçado, J. L. A. Coelho, A. F. Bakuzis, P. C. Morais and D. M. S. Esquivel, *Biophys. J.*, 2000, **78**, 1018.
68 J. Datka and T. Abramowicz, *J. Chem. Soc., Faraday Trans.*, 1994, **90**(6), 2417.
69 P. Fabrizioli, T. Bürgi and A. Baiker, *J. Catal.*, in press.
70 D. G. Rethwisch and J. A. Dumesic, *J. Phys. Chem.*, 1986, **90**, 1625.
71 L. Brabec, M. Jeschke, R. Klik, J. Novakova, L. Kubelkova and J. Meusinger, *Appl. Catal., A*, 1998, **170**, 105.
72 M. Nogami, *J. Mater. Sci. Lett.*, 1993, **12**, 1705.
73 J. A. Weil, J. R. Bolton and J. E. Wertz, *Electron Paramagnetic Resonance*, Wiley, New York, 1994.